International Journal of Multiphase Flow 35 (2009) 195–203

Contents lists available at ScienceDirect

International Journal of Multiphase Flow

journal homepage: www.elsevier.com/locate/ijmulflow

Brief Communication

Measurements of the streamwise vorticity in the wake of an oscillating bubble

Roberto Zenit [a,*], Jacques Magnaudet [b]

[a] Instituto de Investigaciones en Materiales, Universidad Nacional Autónoma de México, Apdo. Postal 70-360 México D.F. 04510, Mexico
[b] Institut de Mecanique des Fluides de Toulouse, 1 Allee du Professeur Camille Soula, 31400 Toulouse, France

ARTICLE INFO

Article history:
Received 27 August 2008
Received in revised form 17 October 2008
Accepted 21 October 2008
Available online 6 November 2008

1. Introduction

Ascending oscillating air bubbles in water have fascinated scientists for many years. Recently found drawings of Leonardo da Vinci (Prosperetti et al., 2003) are now considered the first documented observations of this phenomenon. Small bubbles moving in a low viscosity liquid rise in a straight line; beyond a certain size the bubbles begin to ascend in a zigzag or spiral trajectory. Many studies have been devoted to the subject, especially during the last 50 years (Magnaudet and Eames, 2000). Although the understanding of the causes of this spectacular transition remained unclear for a long time, now its comprehension is nearly complete: the wake behind a spheroidal bubble becomes unstable when the vorticity produced at its surface becomes larger than a certain limiting value (Magnaudet and Mougin, 2007; Yang and Prosperetti, 2007).

The main clues that lead to this discovery arose from both experimental and numerical investigations. Lunde and Perkins (1997) and Brücker (1999) reported the first visualizations of the wake behind oscillating bubbles. Although these studies were not precisely focused to examine the conditions for the transition to unstable trajectory, they showed the existence of vortical structures behind oscillating bubbles, which resembled those observed behind solid spheres. By means of a Schlieren-type technique de Vries et al. (2002), also recently Veldhuis (2007), visualized the wake behind oscillating bubbles. The technique was developed such that the hyper-clean water remained uncontaminated during the experiment. Surface contamination has been found to have a tremendous effect on the critical conditions for transition (Duineveld, 1995). de Vries et al. (2002) found that the wake behind oscillating bubbles was formed by two filaments of counter-rotating streamwise vorticity. They showed that such a vortical structure produced a lift force on the bubble which caused the observed sideways motion. Although the structure of the wake was visible, only limited quantitative results could be obtained. It is not very clear what the proper quantitative interpretation of these visualizations is, since the Schlieren optics show gradients of the refraction index and it is not obvious how to relate these gradients to quantitative values of the velocity or vorticity in the wake.

Approximately at the same time as the experimental observations of de Vries et al. (2002), Mougin and Magnaudet (2002) reported direct numerical simulation results of the motion of a freely ascending fixed-shape spheroid with a stress-free condition at its surface. They found that if the wake behind the bubble remained axisymmetric, the bubble ascended in a straight trajectory; the transition to oscillatory behavior coincided with the appearance of two counter-rotating trailing vortices behind the bubble, in direct agreement with the experimental observations.

The appearance of streamwise vorticity is, therefore, the key for the path instability to occur. Surprisingly, direct experimental measurements of this quantity in the wake behind an oscillating bubble have not been reported to date. The visualizations of Lunde and Perkins (1997) (who used dye) and of Brücker (1999) (who used particle tracers and a PIV system) were not 'clean'; hence, their results could not be used to investigate the nature of the transition for bubbles rising in an uncontaminated liquid. On the other hand, the visualizations of de Vries et al. (2002) and Veldhuis (2007) which clearly showed the appearance of the streamwise vortical structure, provide mostly qualitative information. Hence, it is still necessary to perform 'clean' experiments to measure directly the vorticity in the wake of oscillating bubbles.

In this brief communication, we report measurements of the velocity field in the plane perpendicular to the main bubble motion. From these measurements, the streamwise vorticity was calculated and the structure of the wake was reconstructed. Also, the strength of the vortical structures was measured and the resulting lift force was inferred by two methods (from the trajectory of the bubble and from the strength of the vortices). To our knowledge,

* Corresponding author. Tel.: +52 55 5622 4593; fax: +52 55 5622 4602.
E-mail address: zenit@servidor.unam.mx (R. Zenit).

0301-9322/$ - see front matter
doi:10.1016/j.ijmultiphaseflow.2008.10.007

direct measurements of the streamwise vorticity behind oscillating bubbles have not been reported to date.

2. Experimental setup

Experiments were performed in a cylindrical container of 30 cm height, with a diameter of 10 cm, which is shown schematically in Fig. 1, A careful procedure to minimize contamination was used, described in detail in Zenit and Magnaudet (2008). Air bubbles were produced with a horizontal stainless steel capillary tube, which was inserted through the side wall, and syringe pump.

The liquid used in this investigation was a silicon oil (DMS-T05, polydimethylsiloxane, Gelest Inc.) The properties of the liquid are listed in Table 1. We opted for this liquid because of its low viscosity and because it is formed by a nonpolar molecule which ensures that the gas–liquid interface remains clean under standard laboratory conditions. Recently, we showed (Zenit and Magnaudet, 2008) that this type of liquid can be used to study the transition to oscillatory behavior for millimetric sized air bubbles without the need of an ultrapure environment (Duineveld, 1995).

The shape and vertical terminal velocity of the bubbles were measured using a high-speed camera (APX Photron). Images were obtained at approximately 15 cm above the injection point using a light emitting diode (LED) array which served as a diffuse backlighting illumination. The camera was operated at 1000 frames/s in all cases. Using standard image processing routines (from Matlab), the bubble 'blob' was identified in the $x-z$ (or $y-z$) plane (see reference frame in Fig. 1) and its geometrical center was located and tracked in time to calculate the vertical terminal velocity. In this manner, the bubble equivalent diameter ($d_{eq}=(d_l^2 d_s)^{1/3}$, where d_l and d_s are the long and short bubble diameters, respectively) and the aspect ratio ($\chi=d_l/d_s$) were calculated for each case. Clearly, this technique is sufficient to determine the bubble shape precisely only if the bubbles rise in a straight trajectory. For the case of oscillatory trajectories, the bubble shape could only be obtained when the bubble orientation coincided with the imaging plane.

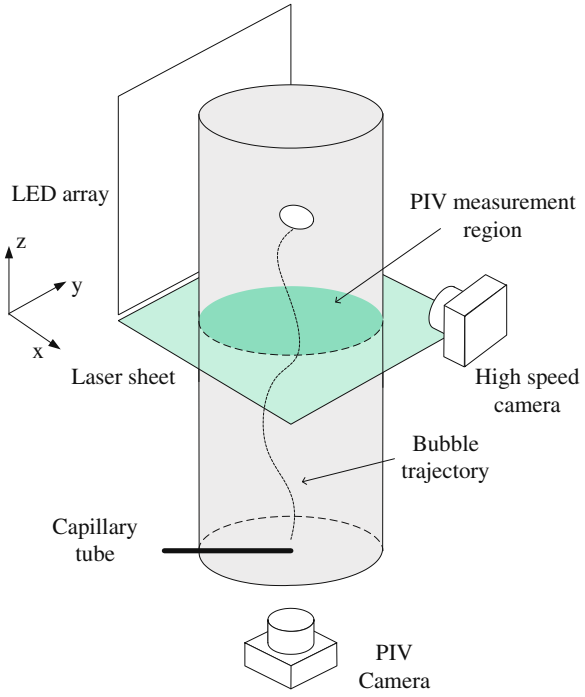

Fig. 1. Scheme of the experimental setup.

Table 1
Properties of the liquid used in the experiment: ρ is the density, μ the dynamic viscosity and σ the surface tension. The properties of pure water are also shown for reference.

Liquid	ρ, kg/m^3	μ, mPa s	σ, mN/m	$Mo=g\mu^4/(\rho\sigma^3)$
Water	1000	1.00	72.86	2.5×10^{-11}
DMS-T05	918	4.59	19.7	6.2×10^{-7}

To investigate the nature of the vortical structures behind moving bubbles, and particularly the streamwise vorticity component, a high-speed particle image velocimetry (PIV) system was implemented to only measure this component. As shown in Fig. 1, the laser plane was aligned horizontally, such that only the velocities in the $x-y$ plane (the reference frame is shown in the figure) could be measured and the streamwise vorticity ω_z be calculated. Hence, the camera was placed below the container and images were obtained at a rate of 400 images/s (also using the APX Photron camera). A NdYag pulsed Laser was used. Great care was taken to prepare the tracer particles. To avoid the reflections from the bubble surface, fluorescent polymer tracer particles of 30 μm were used (from Dantec Dynamics Inc.) To ensure that the addition of the tracers did not contaminate the gas–liquid interface, an elaborate cleaning process was followed. First, the water in which the tracers were suspended was removed by making the suspension pass through a paper filter. The particles were then rinsed and filtered; this process was repeated twice with high-purity methanol and four times with double distilled water. After, the particles were dried with a lamp heater. Once dried, they were rinsed and filtered twice with a low viscosity silicon oil (DMS-T00, from Gelest). Finally, the tracers were suspended in a small quantity of the working fluid (DMS-T05 silicon oil) to be subsequently added to the experiment. To corroborate that the addition of tracer particles did not contaminate the bubble surface, some experiments were conducted using the seeded fluid to measure the bubble terminal velocity (shown below). The bubble velocity and shape were found to be virtually unaffected by the tracers; hence, we can argue that the bubble surface is stress-free in the PIV experiments.

Typical images obtained with the PIV system are shown in Fig. 2. Also, a sequence of images can be viewed in the associated video. The figure shows the two cases that will be studied in detail here. These images were processed with the software Flow Manager (from Dantec Dynamics Inc.) The fluid velocities (u, v) in the $x-y$ plane were obtained for different instants in time. An adaptive cross-correlation technique was used, with a final interrogation area of 32×32 pixels, and an overlap of 50% in both directions. Subsequently, a peak validation, moving average and spacial filter routines were applied. The fluid motion was studied only for times posterior to the passage of the bubble through the plane. Time $t=0$ is set by the time at which the bubble crosses the laser plane: posterior times correspond to positive time values. The curl of the velocity field is the $x-y$ plane was calculated to obtain the streamwise vorticity as

$$\omega_z=\frac{\partial v}{\partial x}-\frac{\partial u}{\partial y}. \tag{1}$$

In addition to the fluid velocity measurements obtained after the bubble has passed through the laser plane, the time evolution of the bubble position in the $x-y$ plane could also be obtained before the bubble crosses the plane. In the video shown along with Fig. 2 it can be observed that prior to the arrival of the bubble in the laser plane, a region devoid of tracers can be clearly identified. This 'shadow' results from the fact that the bubble is in between the light source (the illuminated tracers) and the camera. The shadow can be used to determine the position of the bubble for differ-

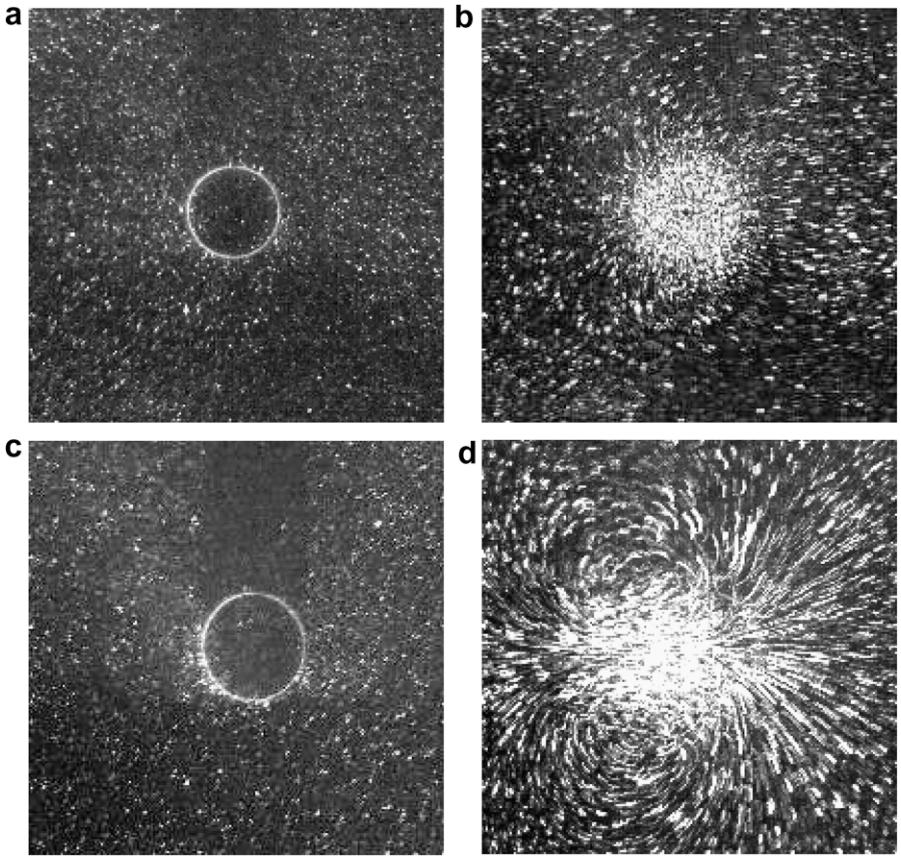

Fig. 2. On the left, images (a and c), are typical images of the PIV plane, at the moment when the bubble crosses the laser plane ($t = 0$). On the right, (b and d), flow streaklines are shown (obtained by superposing images of the flow motion for $t > 0$). (a and c) correspond to cases (S) and (O) of Table 2, respectively. The associated online video shows the fluid motion before and after the bubble passes through the laser plane.

ent times, before the bubble crosses the laser plane. Using image processing tools such as binarization, blob dilation and outline identification (also from Matlab,) the region without tracers was located and its position (geometrical center) was determined in the $x - y$ plane, with an uncertainty of approximately 2%. This information was used, along with the bubble vertical terminal velocity, to calculate the 3D trajectory before the bubble passage through the laser plane.

The image in Fig. 2b (and the corresponding video) shows that the bubble rises in a straight line with no significant vortical motion behind it. On the other hand, for the case of an oscillating bubble (Fig. 2d), the motion occurs in a zigzag manner and the swirling motion of the fluid indicates that the streamwise vorticity component is significant.

3. Results

3.1. Determination of critical conditions

Initially, a series of experiments was conducted to obtain a relation between size, shape and terminal velocity, and also to determine the conditions for transition to an oscillatory trajectory. Some of these data were taken from our previous investigation (Zenit and Magnaudet, 2008). Fig. 3 shows the bubble aspect ratio χ and Reynolds number, calculated as $Re = d_{eq}U_b\rho/\mu$, as a function of the bubble equivalent diameter, d_{eq}. Both Re and χ increase with bubble size, as expected and as predicted by Moore (1965) for the case of perfectly clean spheroidal bubbles. There is a small discrepancy in the Reynolds number, since the experimentally determined value is slightly larger than the theoretical prediction. This difference is a result of the slightly larger velocities measured experimentally. As previously discussed by Duineveld (1995) and Zenit and Magnaudet (2008), bubbles experience a drag force slightly smaller than that calculated by Moore's model, because of their non-perfect spheroidal shape. Nevertheless, since both the aspect ratio and Reynolds number are very close to the predictions of Moore, we can state that the bubble surfaces are clean and, hence, stress-free.

The conditions of transition to an oscillatory trajectory were determined by calculating the standard deviation of the bubble velocity. A bubble was said to be oscillating when the standard deviation of its velocity was larger that 5% of its terminal velocity. In Fig. 3 this condition is depicted by the vertical and horizontal dashed lines. The conditions for transition in this particular liquid are: $d_{eq} = 2.89$ mm, $\chi = 2.10$ and $Re = 110.3$.

Furthermore, experiments were also performed in the liquid with PIV tracers, also shown in Fig. 3. No distinguishable difference can be observed between the measurements with and without PIV tracers. Therefore, we can conclude that the addition of particles did not contaminate the bubble interface.

Based on these results, two cases were chosen to be studied in detail with the PIV system: slightly below and above the transition. These two cases are shown by the asterisk (case S) and filled circle (case O) in Fig. 3, and the corresponding experimental conditions are summarized in Table 2.

3.2. Bubble trajectory

As discussed above, the bubble position in the $x - y$ plane was obtained by further processing of the PIV images: the 'shadow' of the bubble appeared on the images before the bubble itself crossed the laser plane. Fig. 4 shows the $x - y$ position for a bubble ascend-

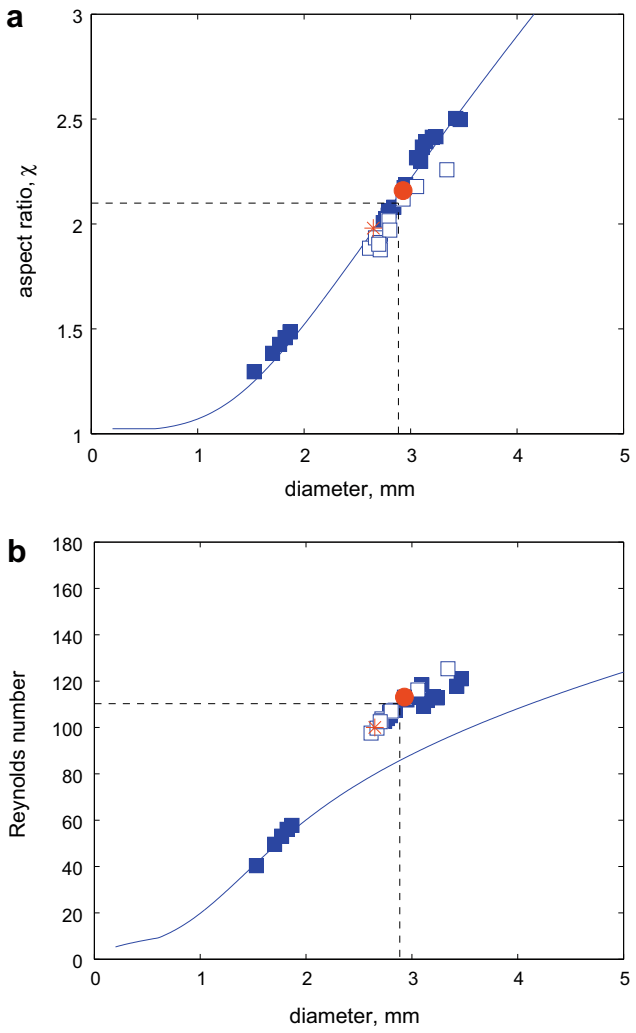

Fig. 3. (a) Bubble aspect ratio, χ, and (b) Reynolds number, Re, as a function of the bubble equivalent diameter, d_{eq}. The empty and solid squares show the results for a liquid with (taken from Zenit and Magnaudet, 2008) and without PIV tracers, respectively. The solid lines show the prediction of Moore (1965). The dashed lines show the critical conditions for transition to an oscillatory trajectory. The asterisk and solid circle show the conditions for the cases (S) and (O) from Table 2.

Table 2
Experimental conditions for the two cases studied in detail.

Case	d_{eq}, mm	$\chi = d_l/d_s$	U_b, mm/s	$Re = U_b d_{eq}\rho/\mu$	$We = U_b^2 d_{eq}\rho/\sigma$
S (straight)	2.65	1.98	188.7	100.0	4.4
O (oscillating)	2.93	2.16	193.1	113.1	5.1

ing in a straight (case S) and an oscillatory trajectories (case O), (a) and (c) respectively. The difference between the two cases is evident.

Note that although the bubble path in (a) is not perfectly vertical, it is notably straight. Some authors have observed such straight-but-not-vertical trajectories for the case of freely ascending light spheres (Jenny et al., 2004). As will be seen below, the wake behind bubbles rising in a straight trajectory does not show a coherent streamwise vorticity structure; hence, the non-vertical trajectory cannot attributed to an effect of the wake. Since the bubble was injected using a horizontal capillary (as shown in Fig. 1), a small initial horizontal motion may have been imposed on the bubble during its release.

On the other hand, the bubble path in (b) shows significant oscillations. The amplitude of oscillation in the y direction is almost seven times larger than that in the x direction: the bubble is moving in a zigzag trajectory or, more precisely, in a very flat spiral.

To reconstruct the 3D trajectory of the bubbles, we considered that the vertical position could be calculated as $z = U_b N_i f$, where N_i is the image number and f is the frame rate. For the results shown here, a fixed value of $f = 400$ frames/s was used. Fig. 4(b) and (d) shows the reconstructed 3D trajectory of the two cases shown in (a) and (c). Both the straight and zigzagging nature of the trajectories is very clear.

3.3. Velocity and vorticity fields

From the images shown in Fig. 2 (and its associated video), a standard cross-correlation technique was applied to obtain the velocity field in the $x - y$ plane. The streamwise vorticity was calculated according to Eq. 1. With these measurements we can observe directly if there is a significant change in the streamwise vorticity between a straight and an oscillating bubble.

Fig. 5 shows the velocity and vorticity fields generated by the oscillating bubble (case O) for several time instants after the bubble has crossed the laser plane. The appearance of two swirling regions of vorticity of opposite sign is very clear. These regions of concentrated vorticity move and their strength reduces in time.

On the other hand, for the case of a bubble rising in a straight line (case S), shown in Fig. 6, the velocity field resembles a 'sink' flow (since the bubble is dragging fluid behind it and across the laser plane), for which the streamwise vorticity is negligible. The wake does not show any significant structure which could explain the straight but not exactly vertical trajectory found for this case. This is why we suspect the detachment of the bubble from the horizontal capillary to be responsible for this small inclination of the path.

3.4. Reconstruction of the wake structure

Now, since we could clearly identify the formation of two regions of streamwise vorticity of opposite sign for case (O), it is possible to reconstruct the structure of the wake behind the oscillating bubble. The measurements of the vorticity field at different time instants are converted into slices of the flow at different streamwise distances (coordinate z) behind the bubble by simply considering that $z = U_b t$. This is clearly an approximation and would only represent the Lagrangian vorticity field behind the bubble for short times (or distances) but, nevertheless, its visualization is instructive.

Figs. 7 and 8 show the reconstructed streamwise vorticity field for case (O). These images show iso-surfaces of ω_z for two values of equal magnitude but opposite sign. Two tubes are observed which extend for approximately seven bubble diameters (for the chosen value of ω_z). The cross-sectional area of the tubes reduces with distance, as the vorticity dissipates due to viscous effects. The bubble trajectory is also shown in the figure. It is important to note that the zigzagging motion occurs in a $x - z$ plane corresponding to that which separates the two vortex tubes. The two vortex tubes are inclined with the same slight inclination as the bubble at $t = 0$. Mougin and Magnaudet (2002) and Magnaudet and Mougin (2007) showed the structure of the streamwise vorticity for the case of oscillating and fixed spheroids. The similarity between the experimental wake and the numerical results is striking. Note, that although the Reynolds number is very different, the aspect ratio is similar. This resemblance further confirms the fact that the aspect ratio, and not the Reynolds number, is the most relevant factor to determine the transition to an oscillatory path (Zenit and Mag-

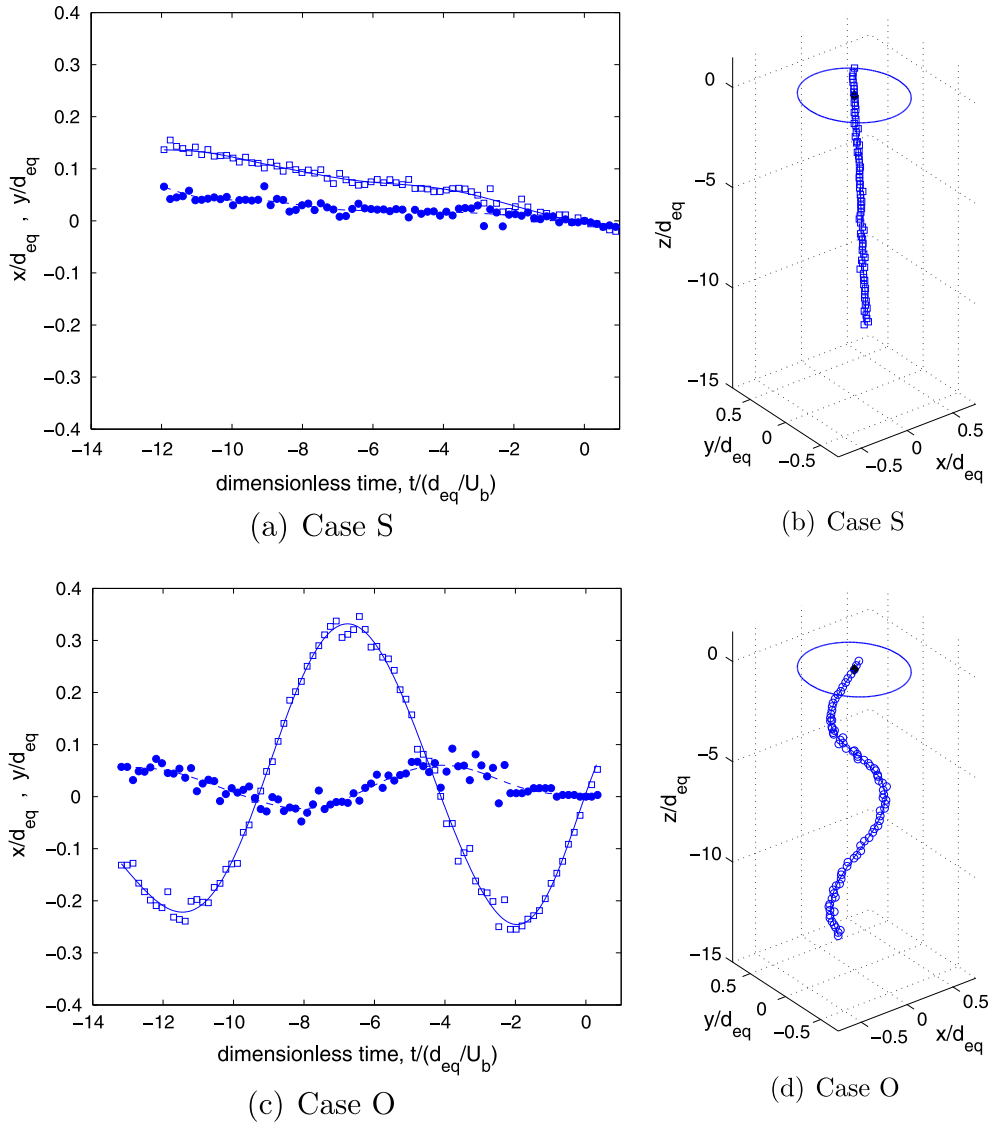

Fig. 4. Bubble trajectories. (a and c) show the position as a function of time: (□), x-position; (•), y-position. Position and time are normalized by d_{eq} and d_{eq}/U_b, respectively. (b and d) show the reconstruction of the tridimensional bubble trajectory. The size of the bubble is shown at (0,0,0), which denotes the position of the bubble center when it crosses the laser plane. The lines, in all cases, show spline fits. (a–b) and (c–d) correspond to cases (S) and (O), respectively, from Table 2.

naudet, 2008), as two bubbles of similar aspect ratio but different Reynolds numbers produce similar streamwise vortical structures.

4. Calculation of the lift force

Using the results presented above, the magnitude of the induced lift force can be determined for the case of the oscillating bubble. The force was calculated from the trajectory of the bubble and from the circulation of the vortices in the wake.

4.1. Lift force inferred from trajectory

The fact that the bubble moves in a non-straight fashion as it ascends (for case O), is an indication that forces in the horizontal direction are present and change in time. Since the three-dimensional trajectory of the bubble was obtained, the evolution of the forces exerted on the bubble can be inferred. By considering similar approaches, Shew et al. (2006) and Veldhuis (2007) calculated the drag and lift (in two directions) forces for both zigzagging and spiralling trajectories. Their analysis was based on a simplification of the generalized Kirchhoff equations expressed in a coordinate system rotating with the bubble.

We used the scheme proposed by Shew et al. (2006) to calculate the lift force. By considering the simplified set of Kirchhoff equations, assuming that the bubble moves with its minor axis always aligned with the velocity vector (as demonstrated by Ellingsen and Risso, 2001; de Vries et al., 2002; Mougin and Magnaudet, 2002; Veldhuis, 2007), the forces on the bubble can be calculated if the pitch and azimuthal angles, θ and ψ, respectively, as defined by Shew et al. (2006), and their time evolutions are known. The lift force in the normal and binormal directions can be calculated from the balance between buoyancy and added mass forces. In other words, the lift force depends on the pitch (or azimuthal) angle, its time variation, the added mass coefficient along the bubble minor axis and the bubble terminal velocity. Details of this calculation can be found in the references above.

The uncertainty in determining the trajectory would, therefore, influence the force calculation. However, as discussed above, with our procedure it is possible to accurately determine the trajectory (within 5% of uncertainty). Also, shape fluctuations could signifi-

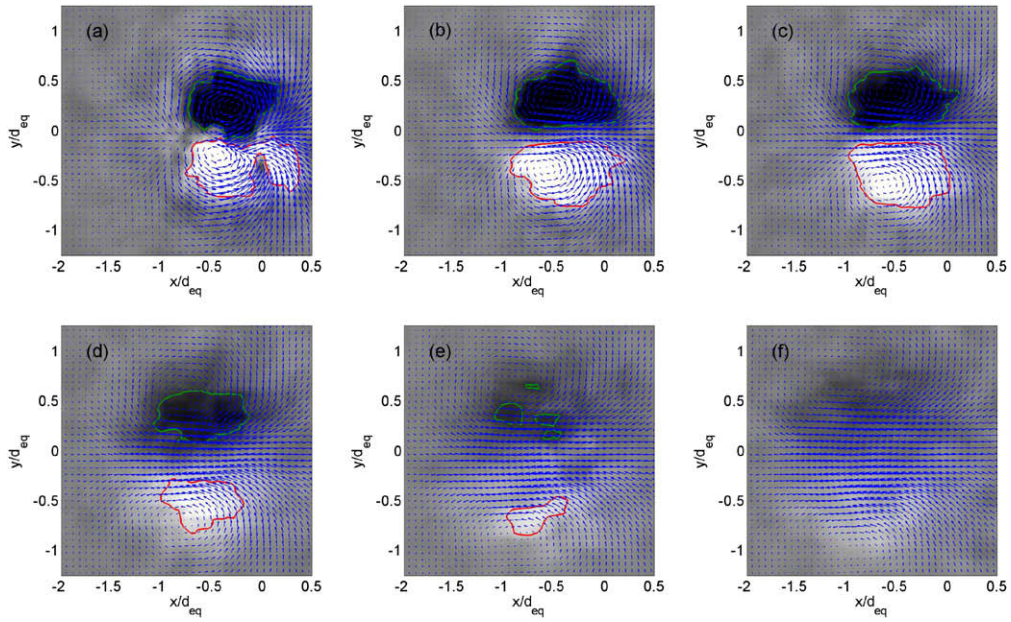

Fig. 5. Velocity and vorticity fields for different times after the bubble has passed the laser plane: bubble rising in a a zigzag trajectory. The arrows denote the velocity vectors in the (x, y) plane. The gray level shows the value of the streamwise vorticity, ω_z: color white (resp. black) denotes a value higher (resp. lower) that $\omega_z/(U_b d_{eq}/2) = +0.20$ (resp. -0.20). The lines show contours of iso-vorticity: green, $\omega_z/(U_b d_{eq}/2) = +0.12$ and red, $\omega_z/(U_b d_{eq}/2) = -0.12$. (a), $t^* = t/(U_b/d_{eq}) \approx 1$; (b), $t^* \approx 2$;(c), $t^* \approx 3$; (d), $t^* \approx 5$; (e),$t^* \approx 7$; (f),$t^* \approx 9$. (For interpretation of the references in color in this figure legend, the reader is referred to the web version of this article.)

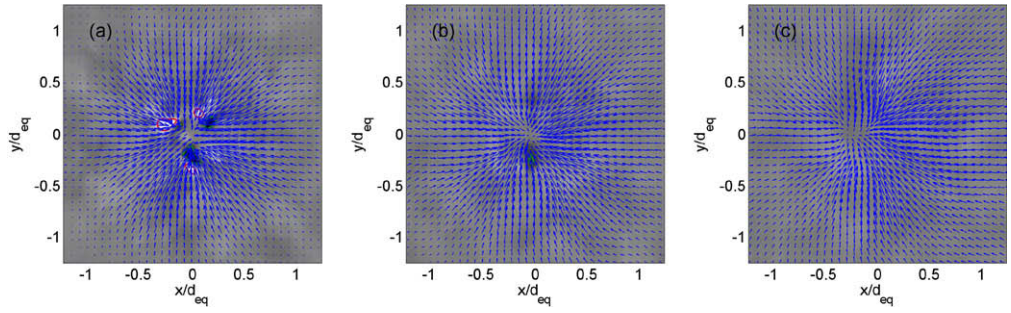

Fig. 6. Velocity and vorticity fields for different times after the bubble has passed the laser plane: bubble rising in a straight trajectory. Gray levels, lines and arrows as in Fig. 5. (a), $t^* = t/(U_b/d_{eq}) \approx 0.7$; (b), $t^* \approx 1.4$; (c), $t^* \approx 2.1$.

cantly affect the force calculation. Both Ellingsen and Risso (2001) and Veldhuis (2007) have shown that for this regime (slightly above the transition to oscillatory behavior), shape fluctuations are small and therefore have a negligible effect.

The pitch angle, θ, varies approximately from -15 to 15 degrees (with respect to the vertical direction) being zero when the bubble's short axis is vertical. Fig. 9 shows the calculated values of the lift force in the 2 and 3 directions (normal and binormal directions, with respect to the direction of the bubble velocity). In this case, the force F_{L2} is greater than F_{L3} because the motion of the bubble is nearly a planar zigzag. The drag force, F_D fluctuates slightly around the value of the buoyancy force. Presumably, the difference between the drag and buoyancy forces results from secondary added-mass effects associated with small changes in the bubble velocity, as noticed by Mougin and Magnaudet (2006) (see their Fig. 3). Other effects, like the lift-induced drag, discussed in detail by Veldhuis (2007), are already included in the total drag force, F_D. When the bubble crosses the laser plane ($t = 0$), the value of θ is approximately 11^o and the horizontal component of the lift force F_{L2} is

$$F_L = F_{L2} \cos\theta = 2.04 \times 10^{-5} N,$$

which is approximately 0.18 times the value of the buoyancy force. Such a force is of sufficient magnitude to affect the path if applied to a nearly massless body, like a bubble. The uncertainty on this estimation, which arises from the determination of the bubble trajectory and aspect ratio, is within 5%.

4.2. Lift force inferred from the vorticity in the wake

It is known that the lift and induced drag on an object can be inferred from the vorticity field in the flow (see for instance Lighthill, 1985). This profound theoretical concept is, however, of limited practical use. For instance, according to the expression given by Howe (1995), to infer the lift force on a bubble, say in the x direction, one would need to know the acceleration of the bubble in the y direction, the vorticity and fluid velocity everywhere outside the bubble in the y and z directions and the *image* vorticity inside the bubble also in the y and z directions.

Therefore, from the measurements obtained in this investigation, it is not possible to completely calculate the lift force acting on the bubble. Alternatively, we can use the model proposed by de Vries et al. (2002), recently revised and used by Veldhuis (2007). This simplified model estimates the force exerted on a bub-

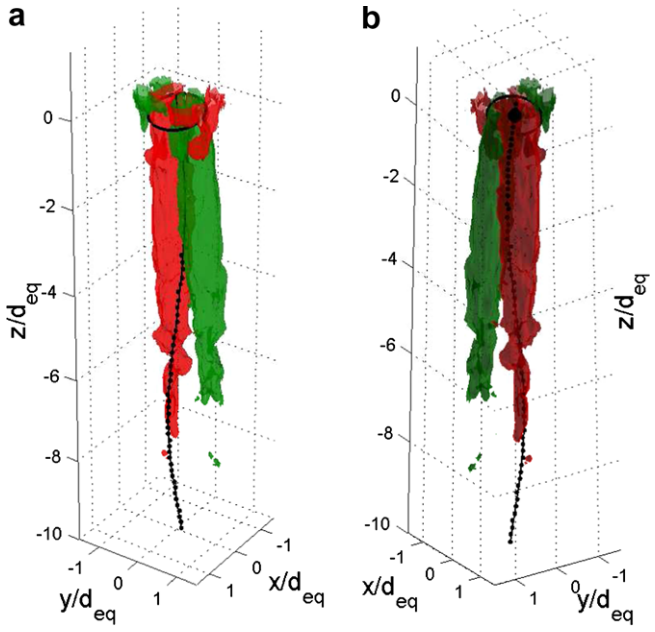

Fig. 7. Reconstructed isovorticity surfaces: the red and green surfaces show iso-streamwise-vorticity surfaces with values of $\omega_z/(2U_b/d_{eq}) = \pm 12.1$. (a and b) show two views of the same flow. The situation shown corresponds to case (O). The line shows the trajectory of the bubble (same data as that shown in Fig. 4d). The profile of the bubble and its orientation are depicted at (0,0,0) by a circle.

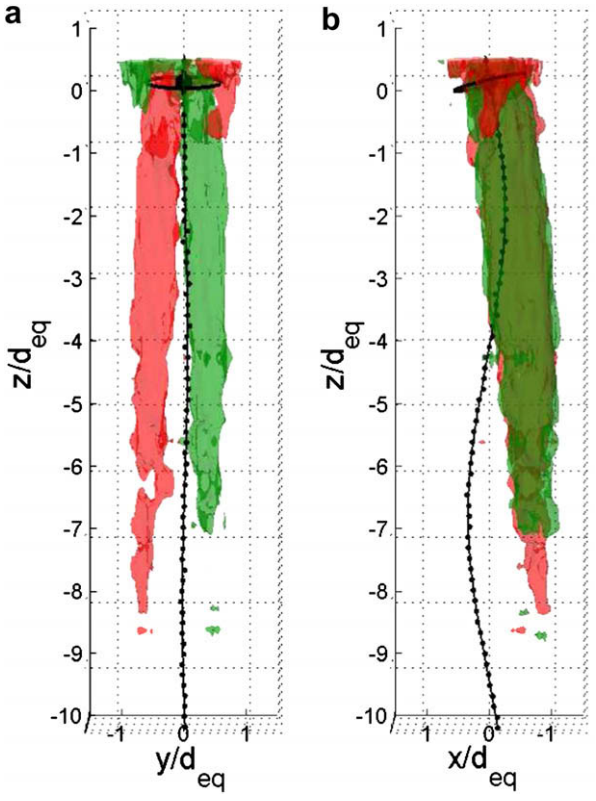

Fig. 8. Reconstructed isovorticity surfaces. All symbols as in Fig. 7.

ble resulting from the velocity field induced by two inviscid vortex tubes. The lift force, F_L is estimated as

$$F_L = \rho \Gamma l_c U_b \tag{2}$$

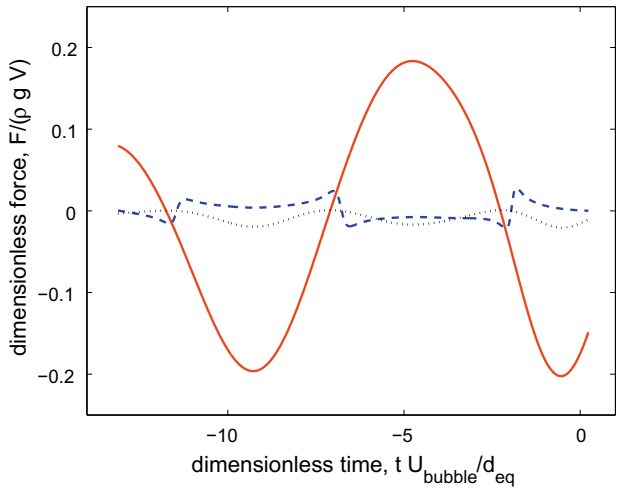

Fig. 9. Forces on the bubble as a function of time obtained from the trajectory shown in Fig. 4d. The solid and dashed lines show the lift forces in the 2- and 3-directions, respectively. The dotted line shows the difference between the drag and buoyancy forces. All forces are normalized by the buoyancy force, $\rho g V$, where V denotes the bubble volume.

where Γ is the strength of the circulation of each of the vortex tubes and l_c is the separation between their centers. This expression gives the lift force for the case of two infinitely long vortex tubes in an inviscid flow. We can use this expression to calculate approximately the lift force on the oscillating bubble since both l_c and Γ can be obtained directly from our measurements.

First, for the case of inviscid vortices, the calculation of the circulation is straightforward because the vorticity is concentrated at the origin of the vortex. The circulation is defined as

$$\Gamma = \int \vec{v} \cdot d\vec{r} = \int_S \omega_z dS \tag{3}$$

where S is an area surrounding the vortex center. For a viscous vortex, the vorticity is not compact; rather it is diffused all around the vortex center as clearly shown in Fig. 5. Although the vorticity is much higher near the center of the vortex, the value of the circulation will depend on the size and shape of S. Moreover, as time progresses, for a given area S, the measured value of Γ decreases with time due to viscous dissipation. Also, the separation distance between the vortex centers changes with time due to vorticity diffusion.

Fig. 10 shows the position of the center of the two vortices as a function of time. This center was calculated on the one hand from the point of maximum vorticity and on the other hand by locating the center of rotation of the velocity field (the point around which streamlines rotate). The two measurements gave approximately the same result. It can be observed in the figure that as time progresses, the separation between the two vortices increases. The distance between centers is $l_c/d_{eq} \approx 0.4$ when the vortices are initially identified and grows to $l_c/d_{eq} \approx 0.8$ for $t^* \approx 10$. The variation of l_c with time follows approximately:

$$l_c/d_{eq} = A + Bt^* + C(t^*)^2$$

where $t^* = t/(d_{eq}/U_b)$ is the dimensionless time and $A = 0.23$, $B = 16.3$ and $C = -42.8$. This result can be compared with the value estimated by de Vries et al. (2002): $l_c/d_{eq} = 0.3$ (with $d_{eq} = 2$ mm), and by Veldhuis (2007): $l_c/d_{eq} = 0.27$ (with $d_{eq} = 1.9$ mm), both of which where obtained from Schlieren visualizations of spiralling bubbles in ultrapure water. Both groups reported a constant value of the separation, regardless of the time or distance from the bubble. Our measurements, even for the initial time, give a value of l_c/d_{eq} larger than that of de Vries et al. (2002) or Veldhuis (2007).

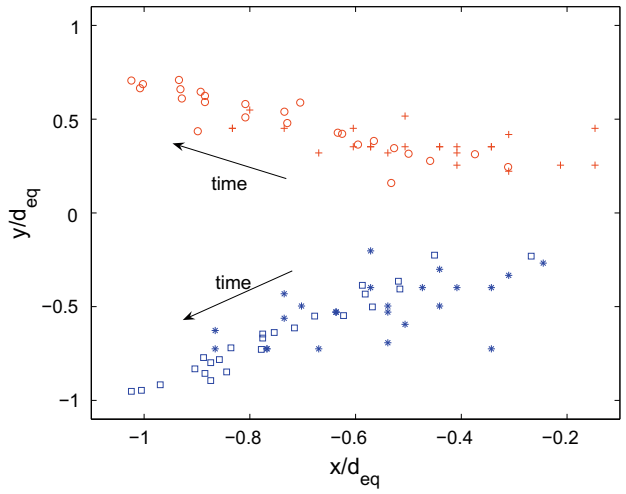

Fig. 10. Normalized position of the center of the two streamwise vortices. The position was calculated by locating the point of highest vorticity: (+) and (∗) correspond to the largest positive and negative values, respectively. The center of the vortices was also located from the center of rotation of the bubble trajectory (from the streamline field): (○) and (□) for the positive and negative vortices, respectively.

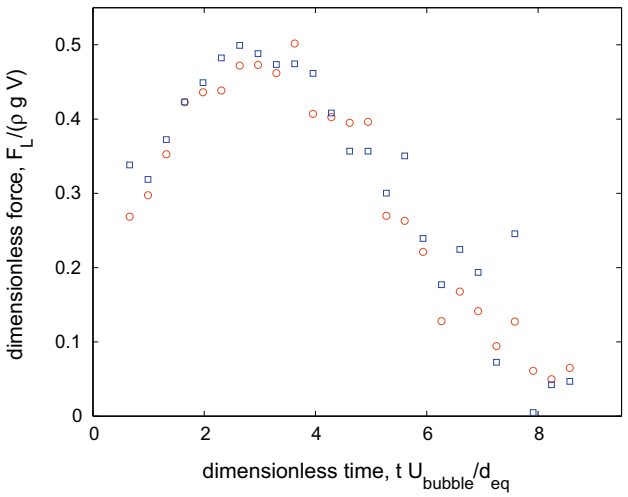

Fig. 12. Force on the bubble as a function of time calculated using Eq. 2. (○) and (□) correspond to the positive and negative vortices, respectively. The lift force is normalized by the buoyancy force, $\rho g V$.

The circulation of the vortices was measured by considering the surface area formed by the contours of iso-vorticity shown in Fig. 5 ($\omega_z/(2U_b/d_{eq}) = \pm 12.1$). In this manner only the region with highest vorticity is considered in the calculation. The measurement is shown in Fig. 11. We find that the measurement of the circulation is robust; a relatively small variation of the circulation is found for different choices of the surface S. For times $t^* < 2$, the measured circulation remains relatively constant and is about 0.28. It then decreases as time progresses. de Vries et al. (2002) obtained $\Gamma/(U_b d_{eq}) \approx 0.21$ which is 25% smaller than the value we determined for times $t^* < 2.0$. Nevertheless, the order of magnitude is similar.

Now, the lift force can be calculated from Eq. 12, using the results shown in Figs. 10 and 11. Since both the separation distance l_c and the circulation Γ change with time, we calculated the value of F_L for different time instants. Strictly speaking, this is not correct since the model is developed for an inviscid vortex with infinite length. The resulting lift force is shown in Fig. 12. Since the distance increases and the circulation decreases with time, a maximum value of the induced lift is found. The normalized lift, $F_l/(\rho g V)$, starts at a value of approximately 0.2, increasing to a maximum about 0.5 at $t^* \approx 3.0$, to then decrease to zero for $t^* > 8$. The mean value of the induced lift is then calculated as

$$\overline{F_L} = \frac{1}{T}\int_0^T F_L(t^*)dt^* = 2.98 \times 10^{-5} N,$$

considering $T = 8$. The obtained value is close to the value calculated from the trajectory of the bubble. It must again be stressed that the calculation of the lift from the vorticity in the wake is an approximation; strictly speaking, one would need the Lagrangian vorticity field behind the bubble. Our reconstruction of the wake is based on Eulerian measurements. Nevertheless, the comparison between the two determinations (trajectory and wake) is fair.

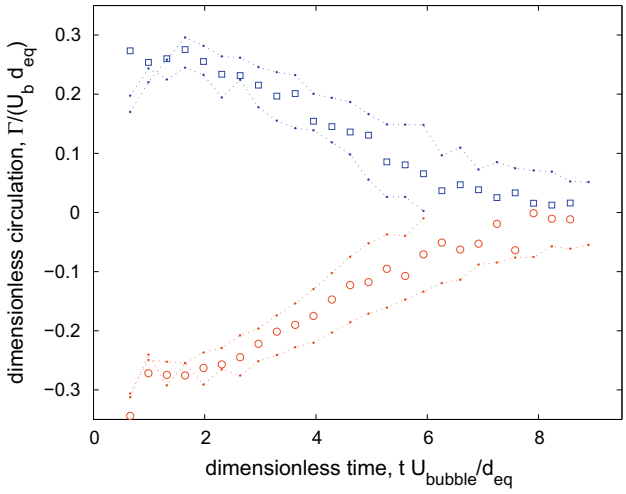

Fig. 11. Dimensionless circulation of the two streamwise vortices calculated according to Eq. 3 considering the area of the iso-vorticity contours shown in Fig. 5, which correspond to $\omega_z/(2U_b/d_{eq}) = \pm 12.1$. (○) and (□) correspond to positive and negative vortices, respectively. The dotted lines show the variation of the measured circulation obtained by considering iso-vorticity contours with $\omega_z/(2U_b/d_{eq}) = 12.1 \pm 4.0$.

5. Conclusions

The mechanism that causes a bubble to ascend in an oscillatory trajectory is now nearly completely understood. The axisymmetric wake becomes unstable when, for large Reynolds number, the bubble aspect ratio exceeds a critical value. The wake then develops two vortex tubes of streamwise vorticity which, in turn, induce a horizontal force on the bubble which causes the sideways motion that characterizes the path instability. Although these vortical structures had been qualitatively observed experimentally and computed numerically in the recent years, an experimental measurement of their strength had never been reported. We performed measurements of the streamwise vorticity in the wake of the bubble using a PIV system maintaining the surface of the bubble clean. The fact that the wake is formed by two counter-rotating vortex tubes of streamwise vorticity was confirmed by direct measurements of the velocity and vorticity fields. Their magnitude was shown to decrease with the distance from the bubble, in very good agreement with previous numerical results. The induced horizontal force inferred from a simple inviscid model was found to be in reasonable agreement with that calculated from the bubble trajectory. In the present case, the magnitude of this force was found to be 20–30% of the buoyancy force.

Among the challenges which remain to fully understand the problem of oscillating bubbles, is the type of trajectory ‘chosen’

by the bubble. Among all possible non-straight trajectories, only zigzags or vertical helices are observed. Moreover, it is not clear how the initial zigzag trajectory slowly evolves to a spiral, i.e. the progressive loss of the planar symmetry of the streamwise vortices needs to be clarified.

These experiments were performed at IMFT during the sabbatical stay of R.Z., who acknowledges the support of the PASPA program of UNAM. The technical assistance of S. Cazin was greatly appreciated.

Appendix A. Supplementary data

Supplementary data associated with this article can be found, in the online version, at doi:10.1016/j.ijmultiphaseflow.2008.10.007.

References

Brücker, C., 1999. Structure and dynamics of the wake of bubbles and its relevance to bubble interaction. Phys. Fluids 11, 1781–1796.

de Vries, A., Biesheuvel, A., van Wijngarden, L., 2002. Notes on the path and wake of a gas bubble rising in pure water. Int. J. Multiphase Flow 28, 1823–1835.

Duineveld, P.C., 1995. The rise of an ellipsoidal bubble in water at high Reynolds number. J. Fluid Mech. 292, 325–332.

Ellingsen, K., Risso, F., 2001. On the rise of an ellipsoidal bubble in water: oscillatory paths and liquid-induced velocity. J. Fluid Mech. 440, 235–268.

Howe, M.S., 1995. On the force and moment on a body in an incompressible fluid, with application to rigid bodies and bubbles at low and high Reynolds numbers. Q. J. Mech. Appl. Math. 48, 401–426.

Jenny, M., Duzek, J., Bouchet, G., 2004. Instabilities and transition of a sphere falling or ascending freely in a Newtonian fluid. J. Fluid Mech. 508, 201–239.

Lighthill, J., 1985. An Informal Introduction to Theoretical Fluid Mechanics. Oxford University Press, Oxford.

Lunde, K., Perkins, R.J., 1997. Observations on wakes behind spheroidal bubbles and particles. ASME Fluids Engineering Division Summer Meeting, paper 3530.

Magnaudet, J., Eames, I., 2000. The motion of high-Reynolds-number bubbles in inhomogeneous flows. Annu. Rev. Fluid Mech. 32, 659–708.

Magnaudet, J., Mougin, G., 2007. Wake instability of a fixed spheroidal bubble. J. Fluid Mech. 572, 311–338.

Moore, D.W., 1965. The velocity of rise of distorted gas bubbles in a liquid of small viscosity. J. Fluid Mech. 23, 749–766.

Mougin, G., Magnaudet, J., 2002. Path instability of a rising bubble. Phys. Rev. Lett. 88, 014502.

Mougin, G., Magnaudet, J., 2006. Wake-induced forces and torques on a zigzagging/spiralling bubble. J. Fluid Mech. 567, 185–194.

Prosperetti, A., Ohl, C., Tijink, A., Mougin, G., Magnaudet, J., 2003. Leonardo's paradox. Appendix to Prosperetti, A. Ohl, C.D. and Tijink, A., 2003. J. Fluid Mech. 482, 271–290.

Shew, W., Poncet, S., Pinton, J.-F., 2006. Force measurements on rising bubbles. J. Fluid Mech. 569, 51–60.

Veldhuis, C., 2007. Leonardo's paradox: path and shape instabilities of particles and bubbles. Ph.D. Thesis, University of Twente.

Yang, B., Prosperetti, A., 2007. Linear stability of the flow past a spheroidal bubble. J. Fluid Mech. 582, 53–78.

Zenit, R., Magnaudet, J., 2008. Path instability of rising spheroidal air bubbles: a shape-controlled process. Phys. Fluids 20, 061702.